FULL PAPER

ADVANCED OPTICAL MATERIALS
www.advopticalmat.d
Check for updates

# Distributed Force Control for Microrobot Manipulation via Planar Multi-Spot Optical Tweezer

*Dandan Zhang,\* Antoine Barbot, Benny Lo, and Guang-Zhong Yang\**

Optical tweezers (OT) represent a versatile tool for micro-manipulation. To avoid damages to living cells caused by illuminating laser directly on them, microrobots controlled by OT can be used for manipulation of cells or living organisms in microscopic scale. Translation and planar rotation motion of microrobots can be realized by using a multi-spot planar OT. However, out-of-plane manipulation of microrobots is difficult to achieve with a planar OT. This paper presents a distributed manipulation scheme based on multiple laser spots, which can control the out-of-plane pose of a microrobot along multiple axes. Different microrobot designs have been investigated and fabricated for experimental validation. The main contributions of this paper include: i) development of a generic model for the structure design of microrobots which enables multi-dimensional (6D) control via conventional multi-spot OT; ii) introduction of the distributed force control for microrobot manipulation based on characteristic distance and power intensity distribution. Experiments are performed to demonstrate the effectiveness of the proposed method and its potential applications, which include indirect manipulation of micro-objects.

## 1. Introduction

Optical tweezer (OT) is an attractive tool that allows indirect manipulation of micro-objects in physics, chemistry, and biomedical studies. OT can provide fine motion control for dielectric micro-particles with sizes up to tens of microns,[1] notably in confined environment.[2] In order to conduct non-invasive

manipulation of cells,[3,4] microrobots, trapped in the focal position of the laser beam can be utilized as end-effectors of the OT.[5] Therefore, developing optical micro-machines to enable dexterous indirect manipulation of OT can have a wide range of applications. For example, four streptavidin-functionalized polystyrene beads, controlled by a time-shared multiplexed OT, have been attached to a biotinylated red blood cell and served as micro-tools to analyze the underlying molecular mechanisms involved in cell flickering.[6] In life science, laser-driven spinning birefringent spheres have been used to generate microfluidic-induced shear force for control of the growth of individual axons (nerve fibers) precisely, paving the way for nerve repair and regeneration.[7] To enable more dexterous indirect optical trapping and optical manipulation, optical microrobotics with novel synthetic structures can be used to increase the flexibility of OT systems and facilitate the deployment of general robotic solutions for biomedical science.[8]

With recent advances in two-photon polymerization and other emerging micro/nanofabrication techniques, steerable non-spherical particles can now be fabricated.[9] Therefore, optically driven microrobots with complex structures can be used for arbitrary translational and angular positioning in 3D space. For example, anisotropic shapes have been considered for the design of micro-particles to create a remotely driven micro-motor based on radiation pressure for micromechanical systems.[10] An indirect optical trapping method using light driven micro-rotors to create a new form of near-field hydrodynamic micro-manipulation has been proposed,[11] with which the 2D trapping of absorbing particles, the control of position and orientation of yeast cells, and the independent control over multiple objects simultaneously have been demonstrated. Apart from using OT to realize reconfigurable hydrodynamic manipulation via the control of optically driven micro-motors, optoelectronic tweezer has been developed to combine dielectrophoresis with OT, which is capable of exerting a stronger manipulation force for a given intensity of light for microrobot control.[12] A shaped particle based on a tapered cylinder fabricated by two-photon polymerization has been proposed for acting as a passive force clamp,[13] which facilitates the design of optically trapped objects with specific force profiles. However, the motions of the passive force clamp are mainly for planar translation. For micro-manipulation which demands

D. Zhang, Dr. A. Barbot, Dr. B. Lo
The Hamlyn Centre
Bessemer Building
Imperial College London
South Kensington, London SW7 2AZ, UK
E-mail: d.zhang17@imperial.ac.uk
Prof. G.-Z. Yang
Institute of Medical Robotics
Translational Medicine Building
Shanghai Jiao Tong University
Dongchuan Road, Shanghai 200240, China
E-mail: gzyang@sjtu.edu.cn

out-of-plane rotation, the structures of the microrobots should be further explored.

In cell surgery applications, cells must be oriented properly to enable the microsurgical tool to access the target components with minimum damage to cells.[14] Therefore, orientation control of biological cells is significant. In traditional biological applications such as intracytoplasmic sperm injection, out-of-plane rotation is generally performed manually by operating two micro-pipettes to repeat vacuum aspiration and release of the mature oocyte until it is oriented at a desired pose.[15] The efficiency and precision for orientation control is limited and prone to manual manipulation errors. The use of microrobots would greatly simplify such tasks. For example, 3D rotation of mouse embryos has been implemented by using a standard holding micropipette to generate a fluidic flow to control the rotation of the oocyte,[16] while using custom-designed microrobots for the 3D rotational control of a single bovine oocyte has been explored by using acoustic levitation.[17] More recently, a multi-functional noncontact micro-manipulation method was proposed based on a vibration-generated whirling flow.[18] However, the proposed methods mentioned above cannot be integrated to OT systems.

For the implementation of out-of-plane control of microrobots via OT, it is worth noting that 3D spatial light modulator (SLM)[19,20] can be used to alter the position of multiple optical traps simultaneously. With SLM, 6D control of microbeads has been realized to manipulate lipid nanotubes by OT in water solutions. An SLM and a pair of galvanometer-mounted mirrors were combined into an OT setup.[21] This provides improved flexibility as the SLM creates an array of traps, which can be moved smoothly and quickly with the galvanometer-mounted mirrors. However, due to the technical complexity involved, this technique is still at a research stage and is not widely employed. Transparent microrobots can be dynamically actuated using a holographic optical tweezer (HOT) based on multiple focused beams of light, each of which can be independently controlled. The out-of-plane rotation can therefore be realized by adjusting the depth of the focal point of different laser traps independently.[22] However, HOT setup is bulky, complex, and expensive.[23] The 6D manipulation implemented in HOT system may be difficult to be transferred to other OT system, such as the easy-to-setup planar OT system based on time multiplexing techniques; more general methods for out-of-plane manipulation should be explored.

To enable versatile micromanipulation for indirect orientation-based control for micro-object manipulation via planar OT, an articulated robot has been built for dexterous cell handling.[24] However, the control relationship between the out-of-plane rotation pose and the position of the laser spots has not been fully explored. The articulated structures may be easily influenced by the fabrication errors while the control resolution is not high enough to realize stable and repeatable out-of-plane pose control. Considering that the trapping force can be influenced by the features of the structure of the targeted microrobot, scalping the shape of the microrobot without adding an articulated structure can be advantageous. To this end, we propose to design a general model for shape modeling of microrobots as well as control strategies to implement out-of-plane rotation along one or multiple axes in the directions that are vertical to the optical axis.

The main contribution of this paper is the structure design of the microrobot and the investigation of two control strategies, which enable the control of out-of-plan rotation of optical microrobots via planar OT. The control input is the range of planar motions or power intensity distribution of the laser spots while the output is the 6D pose of the microrobot. Such optically driven microrobots can be used for complex manipulation in a closed environment, such as a microfluidic chip. It can also assist cell surgery by providing dexterous manipulation. The potential applications include single-cell analysis, embryo injection, nucleus transplantation, organelle biopsy in precision medicine, bottom-up cell assembly for tissue engineering, or other assembly tasks.

The structure design and the control strategies are both applicable to HOT or other types of conventional OT systems, where the focal points of optical traps are limited to the focal plane. Adding more degrees of freedom by using the microrobot design is the first step toward fiber-based optical trap compatible microrobot. Such microrobots can be used as a tool at the tip of a fiber to manipulate micro-objects or implement tissue biopsy using the optical traps generated by multiple optical fibers. Moreover, it can be used as a dexterous tool for lab-on-the-chip to realize cell diagnosis.

## 2. Results and Discussions

### 2.1. Microrobot Design

Spherical and symmetrical shapes are easier to control under OT.[25] Ellipsoids and cylinder-shaped objects have been verified that can be controlled by OT.[26] However, microrobots based on sphere-like shapes and other symmetrical shapes would be difficult to have out-of-plane rotation motion by changing the position of multiple laser spots within conventional OT. Therefore, we try to investigate the design of microrobot which can enable the out-of-plane control by the special configuration of combination of multiple spheres. Overview of the physical mechanism and structure design for microrobot out-of-plane rotation via planar OT is demonstrated in **Figure 1**.

The conceptual design of a microrobot controlled by two optical traps is shown in Figure 1a. The microrobot is developed through the combination of eight micro-spheres as an example. The centers of the micro-spheres which form the microrobot have the shape of an arc. Figure 1b demonstrates the concept of out-of-plane rotation via OT. By trapping two different micro-spheres of the robot, the out-of-plane pose of the microrobot can be altered along one of the axes within the focal plane, which is perpendicular to the optical axis. The number of micro-spheres used to form the microrobot can be varied.

If $n_a$ is the number of micro-spheres which are used to form the microrobot, a series of microrobots can be fabricated with various $n_a$. For example, Figure S1, Supporting Information, shows similar designs of different microrobots generated by different number of micro-spheres ($n_a$ = 8, 11, 15 respectively). $r$ is radius of each micro-sphere. The distance between the two adjacent micro-spheres is $l_1 = 2L\sin\left(\dfrac{\varphi}{2(n_a-1)}\right)$.

**ADVANCED
SCIENCE NEWS**
www.advancedsciencenews.com

**ADVANCED
OPTICAL
MATERIALS**
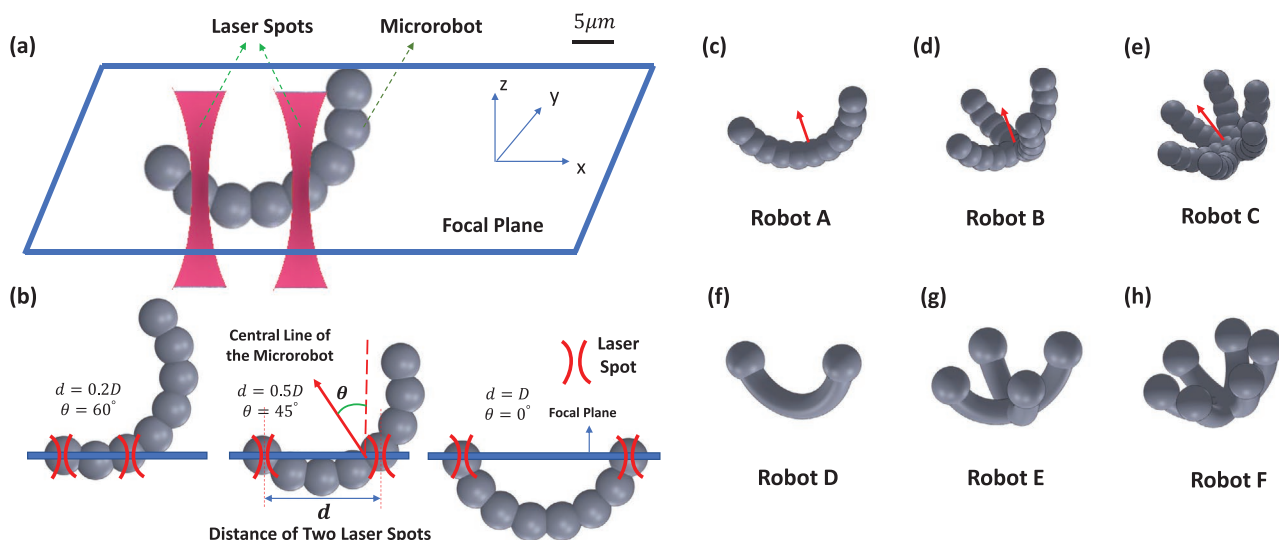www.advopticalmat.de

**Figure 1.** Overview of the physical mechanism and structure design for microrobot out-of-plane rotation via planar OT. a) The conceptual design of a microrobot controlled by two optical traps. b) The demonstration of the out-of-plane rotation concept. c) Modeling of Robot A based on the combination of 11 micro-spheres. d) CAD model of Robot B which can be regarded as a two-arm robot extended from Robot A. e) Design of Robot C which can be regarded as a three-arm robot as an extension of Robot A. f) Design of Robot D which can be extended from Robot A when $n_a \rightarrow \infty$. g) Model of Robot E which can be regarded as a two-arm robot extended from Robot D or extended from Robot B when $n_a \rightarrow \infty$. h) Design of Robot F which can be regarded as a three-arm robot extended from Robot D or extended from Robot C when $n_a \rightarrow \infty$.

Robot A defined in Figure 1c can be regarded as an one-arm microrobot ($n_a = 11$ is used as an example). The central line of the microrobot is indicated by a red arrow. To enable the microrobot to rotate along multiple axes, the structures of Robot B and Robot C (indicated in Figure 1d,e) are proposed. They can be regarded as a two-arm and a three-arm microrobot respectively, which are the extension of Robot design A. Suppose that $n_b$ is the number of arms that the microrobot has, $n_b$-arm microrobot can be developed by rotating the one-arm robot along its central axis. Similarly, the central points of the microsphere of the $n_b$-arm robot can form $n_b$ arcs. The rotating angle between two adjacent arms is $\frac{\pi}{n_b}$.

By defining $D$ as the distance of the central points of two spherical end-effectors on the same arm, that is, a parameter that determines the overall dimension of the microrobot, the distance between two adjacent end-effectors is $l_2 = D \sin\left(\frac{\pi}{2n_b}\right)$. To illustrate the generalizability of the microrobot, a four-arm microrobot can be constructed as well (see Figure S2, Supporting Information).

Suppose that $O_{ij} = [A_{ij}, B_{ij}, C_{ij}](i = 1, 2, ...n_a)$ is the center of the $i_{th}$ micro-sphere which forms the microrobot on the $j_{th}$ arm ($j = 1, 2, ...n_b$), the general mathematical modeling of constructing microrobots for out-of-plane rotation along multiple axes is summarized as follows: For each micro-sphere, we can define the micro-sphere $S = [x, y, z]$ in the Cartesian coordinate as follows:

$$(x - A_{ij})^2 + (y - B_{ij})^2 + (z - C_{ij})^2 = r^2 \tag{1}$$

The center of each micro-sphere can be calculated as follows:

$$A_{ij} = L\cos(\beta_j)\sin(\alpha_i); B_{ij} = L\sin(\beta_j)\sin(\alpha_i); C_{ij} = -L\cos(\alpha_i) \tag{2}$$

where $\left(-\frac{\varphi}{2} < \alpha_i (i=1,2,...n_a) < \frac{\varphi}{2}\right)$ and $(-\pi < \beta_j(j = 1, 2, ...n_b) < \pi)$ are the parameters of the parametric equation, $\alpha_i = -\frac{\varphi}{2} + \frac{\varphi}{(n_a-1)}(i-1)$, $\beta_j = -\pi + \frac{\pi}{(n_b)}(j-1)$. $\alpha_i$ and $\beta_j$ are parameters that determine the relative position of the centers of the micro-spheres, forming the microrobot. We have incorporated more information about parameters $\alpha_i$ and $\beta_j$ in Figure S3, Supporting Information.

Extreme parameters can result in new designs with the same concept but different configurations. For example, when $n_a \rightarrow \infty$, Robot A can transform to Robot D, as shown in Figure 1f. The arms of the microrobot have the shape of a bending cylinder, which is the envelope surface of multiple micro-spheres. Similarly, Robot B and Robot C can be transformed to Robot E and Robot F, respectively, as shown in Figure 1g,h. Robot E and Robot F can also be regarded as the extension of Robot D, which are generated by rotating Robot D along its central line, while the angle between two adjacent arms are $\frac{\pi}{n_b}$.

To perform a micro-manipulation task, the transportation of the microrobot to the target place is important. To increase the trapping radius and the initial moving speed of the microrobot, two spherical structures are added to the end of each arm of the microrobot. Therefore, micro-spheres with $\alpha = \pm\frac{\varphi}{2}$ are defined as end-effectors of the microrobot; the radius ($R$) of these micro-spheres can be increased to enable the microrobot to move at a higher speed, compared to trapping the arm with the shape of a bending cylinder.

The illustration of the structure parameters used in this paper for modeling and the definition of the out-of-plane rotation is shown in **Figure 2**. The radius of the arc is defined as $L$ while the angle is $\varphi$. The key parameters ($\varphi$, $r$, $R$, $D$) used for
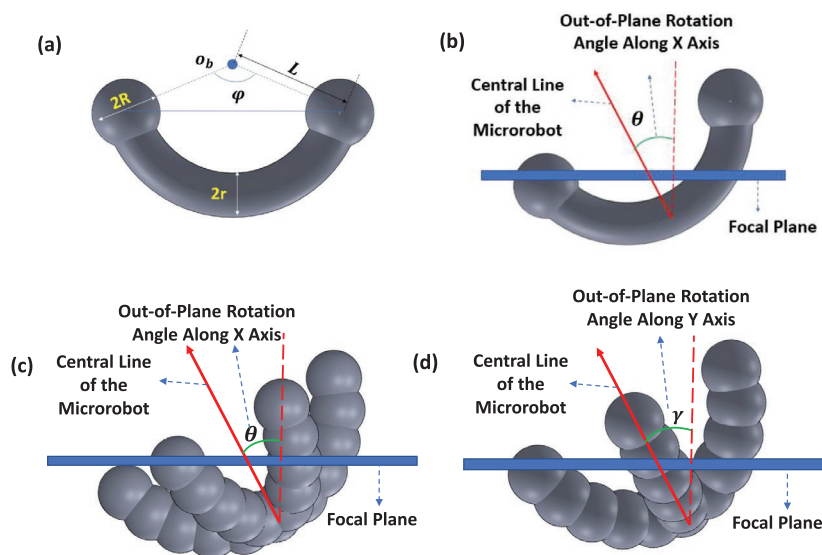
**Figure 2.** The illustration of the structure parameters used in this paper for modeling and the definition of the out-of-plane rotation along one axis or multiple axes in out-of-plane directions. a) Illustration of structure the parameters for modeling. b) The definition of out-of-plane rotation along x axis for Robot D. c) The definition of out-of-plane rotation along x axis for Robot C. d) The definition of out-of-plane rotation along y axis for Robot C.

the structure design are shown in Figure 2a, while the definitions of all the parameters that influence the structure of the microrobot are shown in **Table 1**. Based on the geometric configuration defined, we can have the following equation to illustrate the relationship among $D$, $L$, and $\varphi$.

$$D = 2L\sin\left(\frac{\varphi}{2}\right) \tag{3}$$

To verify the general mathematic description, other design of microrobots using different parameters are shown in Figure S3, Supporting Information. The values of the parameters used to construct the microrobots for experiments are shown in Figure S4, Supporting Information.

To achieve a relatively large range of out-of-plane rotation, $\varphi$ cannot be too small. Therefore, $\frac{3}{4}\pi < \phi < \pi$ is suggested for the general design. The radius of the end-effector should be larger than the micro-spheres which constructs the middle parts of the microrobot. Therefore, $r < R$ is preferred in practice. To enable the microrobot to have a reasonable arm-like shape and make sure that the multi-arm microrobot's end-effectors to

have a reasonable distance, the parameters of $n_a$, $n_b$ $\varphi$, $r$, and $L$ are suggested to meet the following constraints:

$$4r < L < 8r;$$
$$r < L\sin\left(\frac{\varphi}{2(n_a - 1)}\right); \tag{4}$$
$$R < L\sin\left(\frac{\varphi}{2}\right)\sin\left(\frac{\pi}{2n_b}\right)$$

## 2.2. Modeling and Analysis

Ray optics is used for analysis when the wavelength of light is much smaller than the trapped particle. Electric dipole approximation needs to be considered when the diameter of the trapped particle is much smaller than the wavelength of light.[27] For particles much larger than the wavelength (1 µm), geometrical optics is used for the calculation of the optical forces. Since the wavelength of the laser used in this study is 1070 nm while the size of the microrobot is a few microns, we did not consider the electromagnetic effects in this paper. Therefore, we used the geometrical optics approximation to estimate the optical force and torques based on numerical method.

Three assumptions are made before the modeling for optical trapping of microrobot via distributed laser spots.

1) The microrobot can be assumed as a rigid body under the optical force. Therefore, deformation is not considered.
2) The gravity and the buoyancy of the microrobot are small enough to be neglected when the microrobot is trapped by the laser spots.
3) For microrobot with complex shape and dimension much larger than the laser beam waist radius, we assumed that the optical trapping force is generated by specific parts of the overall microrobot, which has the small distance to the nearest laser spots. Therefore, multi-virtual spring system can be used to model the optical trapping force.

The parameters of the stiffness vary with laser power and the dimension of the micro-objects.[28,29] For optical manipulation of a microrobot, the optical trap works only in a small neighborhood around the centroid of a focused light beam. That is to say, the modeling of one trapping force generated by one laser spot can be analyzed within a small region of interest, which can be defined as the targeted trapping component. Due to the Gaussian distribution of light intensity, the trapping stiffness is dependent on the distance between the central point of the targeted trapping component and the central line of the laser spot.[30]

The multi-spot optical trapping modeling can be simplified as a multi virtual spring actuated system. Therefore, for multiple laser spot system, the synthesis optical trapping force is determined as follows:

**Table 1.** The definition of the key parameters for geometric structure construction.

| Parameter | Definition | Parameter | Definition |
|---|---|---|---|
| $r$ | Radius of a micro-sphere | $L$ | Radius of each arc formed by micro-spheres |
| $R$ | Radius of the end-effector | $\varphi$ | Angle range of each arc formed by micro-spheres |
| $n_a$ | Number of micro-spheres on each arm | $n_b$ | Number of arms for a microrobot |

**2000543 (4 of 15)**

**ADVANCED
SCIENCE NEWS**

www.advancedsciencenews.com

**ADVANCED
OPTICAL
MATERIALS**

www.advopticalmat.de

$$F_t = \sum_{i=1}^{n} k_i(d) (p_i - q) \tag{5}$$

where $p_i$ is the position of the focus of the $i_{th}$ laser beam, $q$ represents the position of the targeted trapping component, $d = \|p_i - q\|$ is the relative position between the targeted trapping component and the centroid of the laser beam, while $k_i$ is the spatially varying trapping stiffness of the $i_{th}$ spot.

$$k_i(d) = k_c \quad (d < R_c);$$
$$k_i(d) = k_c e^{-(d-R)^2} \quad (d \geq R_c) \tag{6}$$

$R_c$ denotes the trapping radius, which is a parameter that defines a region where the constant spring theory can work well. $k_c$ is a stiffness constant. $k_c$ and $R_c$ can be roughly estimated through simulation.[31] It can be observed that when $d \gg R_c$, $k_i \to 0$.

We denote the optical trapping force generated by the laser beams exerted on the microrobot is $F_r$ in the transversal plane and $F_z$ in the longitudinal plane, respectively. The torque generated to control the out-of-plane rotation is $M_t$. The stiffness in the longitudinal and the transversal direction may be different. Therefore, we denote that $k_{zi}$ is the longitudinal stiffness constant for the $i_{th}$ critical component, $k_{ri}$ is the transversal stiffness constant for the $i_{th}$ critical component, $R_{cri}$ is the transversal trapping radius, while $R_{czi}$ is the longitudinal trapping radius.

A complex shape microrobot can be assumed to be the combinations of several basic components, such as a cylinder, sphere and ellipsoid. The surface of the microrobot can be regarded as the combination of many planes through triangulation. In this way, numerical calculation can be used to estimate the stiffness of the microrobot, as the relationship between the incoming ray and the reflective ray is known. After several transmission and reflection, the energy of the laser is reduced and the iteration terminates. The total optical force $F_i$ exerted by the focused beam on the targeted component is then the sum of all the rays' contributions.

The optical force ($F_i$) applies on the targeted trapping component for different positions of its center along the $x$ axis in the transversal plane near the focal point can be calculated based on the geometrical optics approximation using a computational toolbox (Optical Tweezers in Geometrical Optics).[32] Therefore, the transversal stiffness constant $k_{cr} = \left.\frac{\partial F_i}{\partial r}\right|_{(r=0)}$ can be obtained. Similarly, $k_{cz} = \left.\frac{\partial F_i}{\partial z}\right|_{(z=0)}$ can be calculated. The parameters for the numerical calculation can be found in Table S1, Supporting Information. For the spherical end-effector with radius $R = 1.2\,\mu m$, the transversal trapping stiffness constant is $k_{cr} = 136.9 pN\,\mu m^{-1}$, while the longitudinal stiffness is $k_{cz} = 56.5 pN\,\mu m^{-1}$. As for the trapping radius, the transversal trapping radius is $R_{cr} = 1.14\,\mu m$, while the longitudinal trapping radius is $R_{cz} = 1.20\,\mu m$. Based on these parameters and Equations (5) and (6), the trapping force can be obtained. The trapping force profile of the spherical end-effector can be viewed in Figure S5, Supporting Information, while the calculation and trapping force profile of the micro-sphere with radius $r = 0.96\,\mu m$ is shown in Figure S6, Supporting Information.

In order to quantify the effectiveness of the transfer of momentum from the ray to the microrobot, the trapping efficiency can be utilized. It is described by the ratio between the modulus of the optical force and the momentum per second of the incoming ray. The transversal and the longitudinal trapping efficiency of the spherical end-effector are shown in Figures S7 and S8, Supporting Information, respectively. For a multi-spot system, the transversal and longitudinal synthesis trapping force are determined by Equation (7), while the torque can be estimated by Equation (8).

$$F_r = \sum_{i=1}^{n} k_{ri} \times (p_{ri} - q_{ri}), \quad F_z = \sum_{i=1}^{n} k_{zi} \times (p_{zi} - q_{zi}) \tag{7}$$

where $p_{ri}$ and $q_{ri}$ represent the position of the laser spot and the critical structure in the transversal plane respectively. $p_{zi}$ and $q_{zi}$ represent the position of the laser spot and the critical structure in the longitudinal plane respectively. $n$ is the number of laser spots.

$$M_t = \sum_{i=1}^{n} k_{zi} (p_{zi} - q_{zi}) \times q_i + \sum_{i=1}^{n} k_{ri} (p_{ri} - q_{ri}) \times q_{zi} \tag{8}$$

By using time multiplexing, multiple laser spots can form a distributed force control system by changing the configuration of the laser spots, which includes the relative position and the distributed power of the spots. $\theta$, $\gamma$, $\phi$ represents the roll, pitch, and yaw orientation angle between the body reference frame and the global reference frame along the $x$, $y$, $z$ axes, respectively. The rotation along the $z$ axis can be regarded as planar rotation, the implementation is illustrated in Figure S9, Supporting Information. $\theta$, $\gamma$ are regarded as the out-of-plane pose, which can be changed by varying the configuration of the distributed laser spots. The control strategy therefore needs to be explored, which determines the relationship between the pose of the microrobot and the configuration of the distributed force control system.

## 2.3. Distributed Force Control Strategy

Distributed force control represents the control of the out-of-plane pose of the microrobot by varying the configuration of the distribution of the laser spots. The microrobot can be trapped in a fixed focal plane, the motion of which can be controlled by changing the position and power intensity of the multiple laser spots based on a predefined principle. Since the configuration of the distributed laser spots can be adjusted, the force and torque distribution can be varied, thus the microrobot can stay at a new equilibrium position with different out-of-plane poses. Therefore, two typical control strategies are proposed in this section, which indicates that the out-of-plane pose of the microrobot can be controlled by characteristic distance and the power intensity distribution. The illustration of the distributed force control strategy is shown in **Figure 3**.

*Control Based on Various Characteristic Distance (Control Strategy A):* The first control strategy is based on characteristic distance, which can be realized when the targeted trapping points of the microrobot are coincided with the focus of
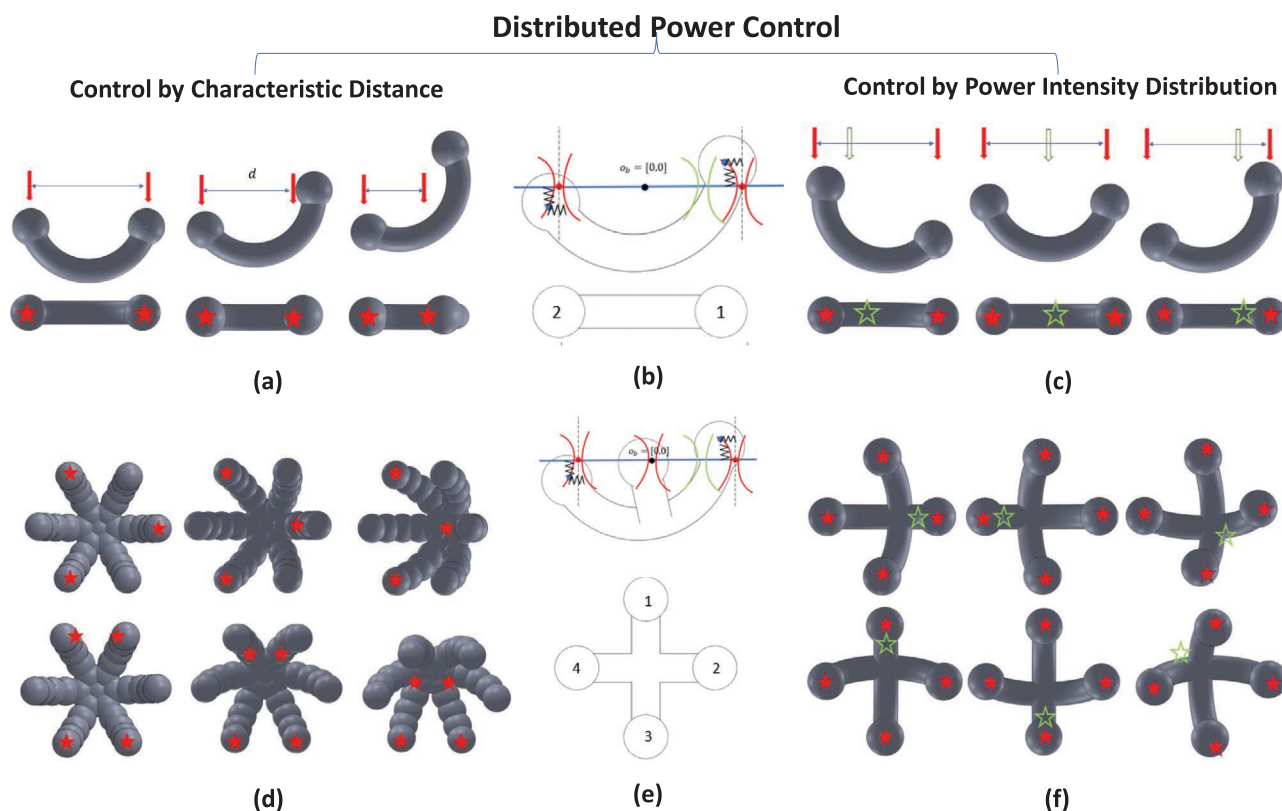
**ADVANCED
SCIENCE NEWS**
www.advancedsciencenews.com

**ADVANCED
OPTICAL
MATERIALS**
www.advopticalmat.de

**Figure 3.** Illustration of the distributed force control strategy. (a) Illustration of the characteristic distance based control for the one-arm microrobot. (b) Illustration of the virtual spring theory for the one-arm microrobot control. (c) Illustration of the out-of-plane control for the one-arm microrobot based on various power intensity distribution. (d) Illustration of the characteristic distance based control for the two-arm microrobot. (e) Illustration of the virtual spring theory for the two-arm microrobot control. (f) Illustration of the out-of-plane control for the two-arm microrobot based on various laser power intensity distribution.

the laser spots. This means that $p_{zi} = q_{zi}$ ($i = 1, 2, ...n$) and $p_{ri} = q_{ri}$ ($i = 1, 2, ...n$). Therefore, $F_r = 0$, $F_z = 0$, and $M_t = 0$ can be reached according to Equations (7) and (8). For the control strategy based on changing the characteristic distance, the geometric constraint of the microrobot can be used to estimate the control relationship between the overall out-of-plane pose and the characteristic distance. There are $2 \times n_b$ directions for the implementation of dexterous out-of-plane rotation for $n_b$-arm microrobot. For out-of-plane control along each axis, the minimum number of laser spots to control the microrobot is two. As for out-of-plane rotation along multiple axes, the minimum number of laser spots to control the microrobot is three, while adding more laser spots can enhance the dexterity of control.

*Control Based on Various Power Intensity Distribution (Control Strategy B)*: The second control strategy is based on power intensity distribution. Although the out-of-plane control along multiple axes can be realized by adjusting the characteristic distance of the laser spots, the dexterous manipulation is restricted to specific axes. To increase the stability and the generality of the control principle, a power intensity distribution control strategy is proposed. This means that more optical traps can be added to form the distributed force control system. A fixed pattern is used to form the basic configuration of $2 \times n_b$ laser spots while the position and the ratio of the power intensity of

a laser spot compared to the other laser spots can be varied to control the out-of-plane pose of the microrobot. In this case, $p_{zi} \neq q_{zi}$ ($i = 1, 2, ...n$) and $p_{ri} \neq q_{ri}$ ($i = 1, 2, ...n$). The control of the microrobot can still be realized, which is determined by the virtual spring theory mentioned in the previous section.

The two control strategies mentioned above are explored for out-of-plane rotation along a single axis at first. Further studies are conducted on out-of-plane rotation along multiple axes, which enables the implementation of 6D dexterous control.

### 2.3.1. Rotate the Microrobot Along One Axis in Out-of-Plane Direction

*Control Based on Various Characteristic Distance (Control Strategy A)*: For a one-arm microrobot, two laser spots can be used to trap the microrobot based on the control of changing characteristic distance. In this case, $p_{zi} = q_{zi}$ ($i = 1, 2, ...n$) and $p_{ri} = q_{ri}$ ($i = 1, 2, ...n$), the influence of the stiffness of the laser spot is not significant, since $F_r = 0$, $F_z = 0$, and $M_t = 0$ can always be reached.

The definition of out-of-plane pose of Robot D is illustrated in Figure 2b, while the out-of-plane rotation of Robot D controlled by various characteristic distance is illustrated in Figure 3a as an example, including the microrobot front view

ADVANCED
SCIENCE NEWS
www.advancedsciencenews.com

ADVANCED
OPTICAL
MATERIALS
www.advopticalmat.de

and top view at various out-of-plane poses. The red arrows in the figures indicate the optical axis directions in the front view while the red stars indicate the position of the optical traps in the top view. The microrobot can have various out-of-plane pose by adjusting the distance between two laser traps for out-of-plane rotation along one axis. The definitions of out-of-plane pose of Robot C along $x$ axis and $y$ axis are illustrated in Figures 2c and 2d, respectively.

To make the shape of the control curve invariant to the microrobot dimension, we define characteristic distance $d^* = \frac{d}{D}$. The aim of the modeling for the control based on characteristic distance is to find out the relationship between the distance of the two laser spots and the out-of-plane pose ($\theta$) of the microrobot. When the microrobot has pose $\theta = 0°$, its end-effectors can be trapped by two laser spots simultaneously ($d = D$), and thus translation motions and planar rotation can be easily achieved.

For the out-of-plane pose control of Robot D, we can assume that one laser spot keeps trapping one spherical end-effector, while another laser spot is moving but trapping part of the cylindrical arm of the microrobot during the out-of-plane rotation. The relationship between $L$, $\varphi$, $\theta$, and $d$ is illustrated by Figure S10, Supporting Information. In this way, the out-of-plane rotation can be realized while the relationship between $\theta$ and $d$ is determined as follows:

$$\theta = \frac{\varphi}{2} - \arcsin\left(\frac{d}{2L}\right) \tag{9}$$

Therefore, the relationship between $d^*$ and $\theta$ is described as follows:

$$\theta = \frac{\varphi}{2} - \arcsin\left(d^* \sin\left(\frac{\varphi}{2}\right)\right) \tag{10}$$

*Control Based on Various Power Intensity Distribution (Control Strategy B)*: As for the power intensity distribution control, the position of an additional laser spot can be added to alter the power distribution and therefore enabling the control of the microrobot. The overview of the control strategy based on the power intensity control is illustrated in Figure 3c. The two red stars represent the fixed laser spots while the green star represents the moving laser spot, whose position and power intensity is adjustable.

Suppose that the position of the first fixed laser spot is $P_1 = \left[-\frac{D}{2}, 0\right]$, the position of the second fixed laser spot is $P_2 = \left[\frac{D}{2}, 0\right]$, the position of the moving laser spot is $P_3 = [x^*, 0]$ in the $x - z$ plane, while the original central point of the microrobot is $P_0 = [0, 0]$. $m$ is a parameter for controlling the relative laser power intensity ratio between the moving laser spot and the fixed laser spot. The main contribution to the overall trapping force is from the spherical end-effector. The concept for the virtual spring theory is illustrated in Figure 3b. In this case, $d^* = \frac{2x^*}{D}$. Assume that $R^*$ is the threshold of distance to determine the effectiveness of virtual spring theory. Therefore, we can obtain the following relationship:

$$\theta = \arccos \frac{md^* + (2 + 2m)}{-\frac{k_z}{k_r}(2 + 2m) + (2 + 2m)} \qquad (R^* \leq d^*);$$

$$\theta = e^{pd^*} \qquad (d^* < R^*) \tag{11}$$

where $p$, $R^*$ and $K^* = \frac{k_z}{k_r}$ are parameters that shall be tuned empirically through experiments. The proof can be found in Proof 1, Supporting Information.

### 2.3.2. Rotate the Microrobot Along Multiple Axes in Out-of-Plane Directions

*Control Based on Various Characteristic Distance (Control Strategy A)*: For out-of-plane rotation along multiple axes, Robot C is used as an example; the out-of-plane rotation angle of $\theta$ and $\gamma$ are defined in Figure 2c,d. The out-of-plane control strategy based on various characteristic distance for Robot C in two directions is shown in Figure 3d. The microrobot can be trapped in a fixed focal plane, the motion of which can be controlled by changing the position of multiple laser spots. The minimal number of required laser spot is three in this case. Though the position of multiple laser spots can be adjusted at the same time, the most simple method is moving one laser spot while the other two laser spots remain in the original position.

For the out-of-plane rotation along the $x$ axis, three laser spots ($P_i$ ($i = 1, 2, 3$)) are used to trap three spherical end-effectors of the microrobot simultaneously in the initial status. Suppose that $P_2$ and $P_3$ are fixed after the robot being trapped, the central point of which is defined as $P_r = [x_r, y_r]$. Based on the geometric relationship, $\|P_2 - P_3\| = \frac{\sqrt{3}}{2}D$. The control input (characteristic distance) $d^* = \frac{\sqrt{(x_1 - x_r)^2 + (y_1 - y_r)^2}}{D}$ is adjusted by moving the position of $P_1$.

The relationship between $\theta$ and $d^*$ can be expressed as follows:

$$d^* = -\frac{1}{2}\left[\cot\left(\frac{\varphi}{2}\right)\sin(\theta) - \frac{1}{2}\cos(\theta)\right] + \frac{1}{2}\sqrt{\left[\cot\left(\frac{\varphi}{2}\right)\sin(\theta) - \frac{1}{2}\cos(\theta)\right]^2 + \frac{3}{4}} \tag{12}$$

The proof can be found in Proof 2, Supporting Information. The inverse function of $\theta = f(d^*)$ exists, and is plotted in Figure 6b.

As for the out-of-plane rotation along the $y$ axis (see Figure 3d), four laser spots are used to control the pose of the microrobot based on the characteristic of the shape from the top to down view. We denote the angle for out-of-plane rotation along the $y$ axis as $\gamma$. Suppose that $P_3$ and $P_4$ are fixed after the robot being trapped. Based on the geometric relationship, $\|P_3 - P_4\| = \frac{D}{2}$.

The control input $d^* = \frac{\sqrt{\left(\frac{(x_1 + x_2)}{2} - \frac{(x_3 + x_4)}{2}\right)^2 + \left(\frac{(y_1 + y_2)}{2} - \frac{(y_3 + y_4)}{2}\right)^2}}{D}$ is adjusted by moving the position of $P_1$ and $P_2$. The relationship between $\gamma$ and $d^*$ can be expressed as follows:

$$d^* = -\frac{1}{2}\left[\cot\left(\frac{\varphi}{2}\right)\sin(\gamma) - \frac{\sqrt{3}}{2}\cos(\gamma)\right]$$
$$+ \frac{1}{2}\sqrt{\left[\cot\left(\frac{\varphi}{2}\right)\sin(\gamma) - \frac{\sqrt{3}}{2}\cos(\gamma)\right]^2 + \frac{1}{4} - 2\sqrt{3}} \tag{13}$$

The proof can be found in Proof 3, Supporting Information. The inverse function of $\gamma = f(d^*)$ exists, and is plotted in Figure 6c. Similarly, the out-of-plane rotation concept for Robot B can be found in Figure S11, Supporting Information.

*Control Based on Various Power Intensity Distribution (Control Strategy B)*: The power intensity distribution control strategy for Robot E is illustrated in Figure 3f as an example. A fixed pattern is used to form the basic configuration of four laser spots for the two-arm microrobot while the position and the ratio of the power intensity of a laser spot compared to the other laser spots can be varied to control the out-of-plane pose of the microrobot.

The control relationship between the distance of the four laser spots and the out-of-plane rotation angle for Robot E is described as follows:

$$\theta = \arccos \frac{2md^* + (4+m)}{-\frac{k_z}{k_r}(4+3m) + (4+3m)} \quad (R^* \leq d^*);$$
$$\theta = e^{pd^*} \quad (d^* < R^*) \tag{14}$$

where $p$, $R^*$, and $K^* = \frac{k_z}{k_r}$ are parameters that needed to be tuned by experiments. The proof can be found in Proof 4, Supporting Information. The power intensity distribution control can be easily extended to $n_b$-arm robot. Comparisons among using different parameters for the modeling of the power intensity distributed control for Robot B are shown in Figure S12, Supporting Information.

### 2.4. Microrobot for Indirect Manipulation

Micro object immobilization is essential for observation and measurement of a target object in microscale, while transportation to a targeted position is required for micro-assembly task when the visual field is small and the workspace is limited. Moreover, to observe or operate the micro-object in different directions, it is desirable to control the pose of the targeted micro-object. Therefore, optically actuated microrobots are investigated in this paper to be used as the tools for indirect manipulation of micro-object with out-of-plane rotation. The design and potential applications of microrobot with body are illustrated in **Figure 4**.

For micro-object handling, microrobots with additional components to assist the out-of-plane rotation of micro-objects are worth studying. Considering that the microrobots designed in Figure 1 can act as the platform to mount various micro-tools for potential actuation or sensing functions, the design of Robot D is extended as an example.

Robot G is constructed by combining Robot D with two plate-like grippers on both sides, as shown in Figure 4a. Robot G is capable of holding spherical shape micro-objects. Two microrobots can be used to transport or rotate a
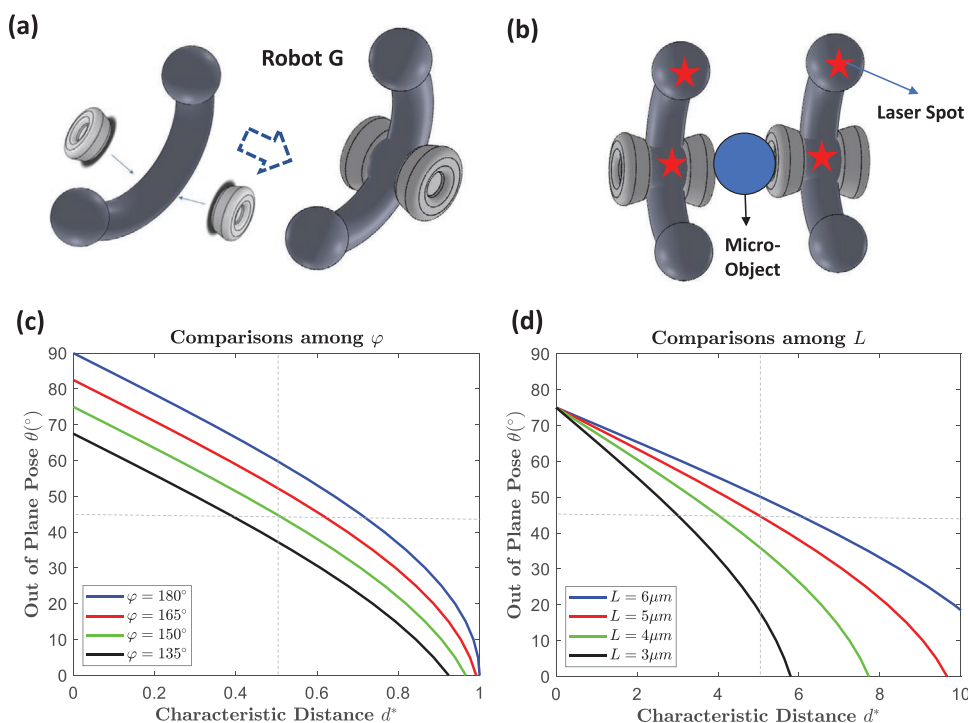


**Figure 4.** Design and potential applications of microrobot with body and grippers. a) Comparisons of the relationship between $\theta$ and $d^*$ using different $\varphi$. b) Comparisons of the relationship between $\theta$ and $d^*$ using different $L$. c) The new design of Robot G as an extension of Robot D with two additional holders. d) Potential application of using two microrobots to cooperatively rotate a micro-object.
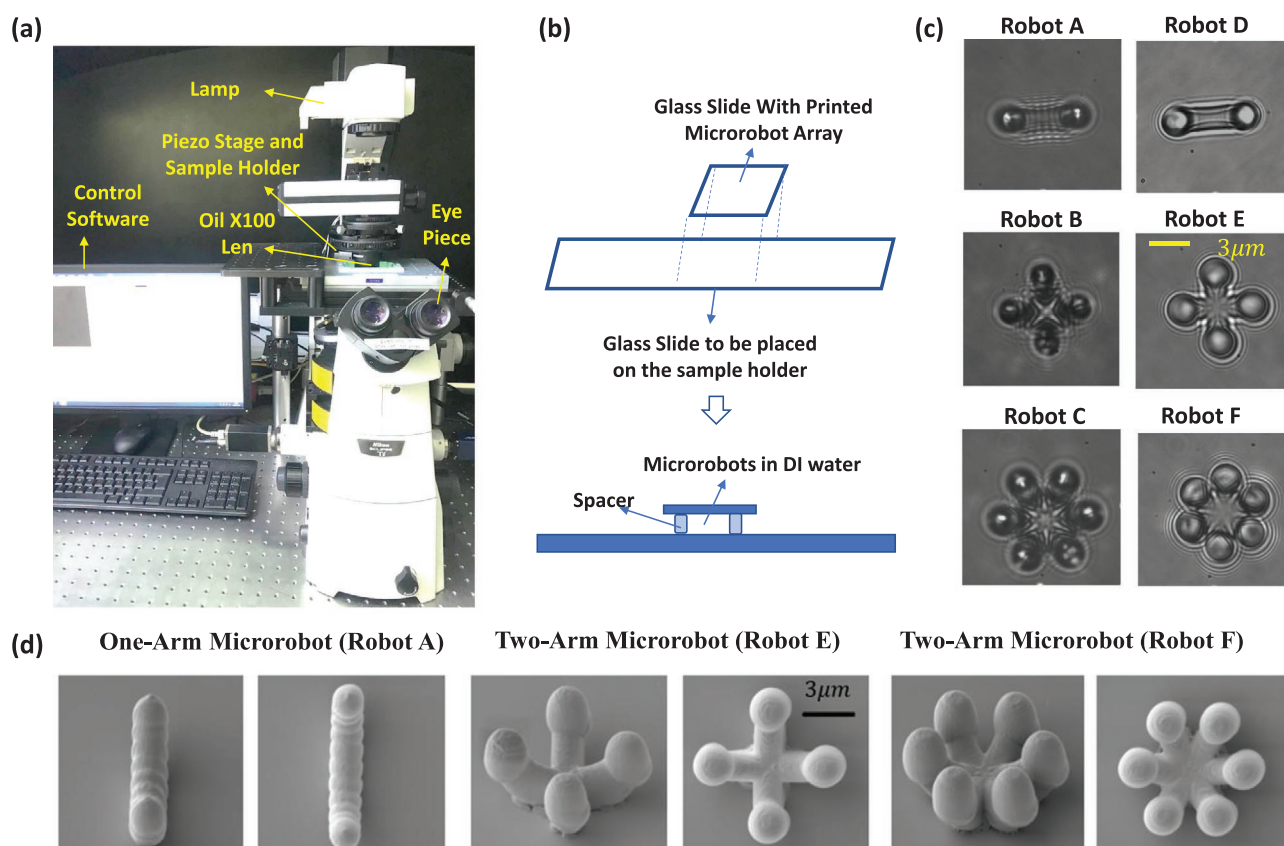
**2000543 (8 of 15)**

**Figure 5.** An overview of the microrobots and their experimental environment. a) The physical optical tweezer system. b) The schematic diagram of the environment for microrobot operation. c) Microscopic view of the Robot A-F for manipulation with OT. d) Different views of the SEM images of three typical microrobots with different number of arms.

micro-object cooperatively for observation; the concept demonstration is shown in Figure 4b.

$\varphi$ and $L$ can influence the shape of the control curve directly. The dimension of the microrobot can be adjusted based on the targeted application requirements. Using the out-of-plane rotation, different views of the micro-object can be observed. Comparisons between different $\varphi$ is shown in Figure 4c. After drawing a referenced line in the figure, we pick up the curves that cross the central point of the graph. Therefore, $\varphi = 150°$ is used in this paper. The differences of the control curve with different $L$ are shown in Figure 4d. $L$ controls the overall dimension of the microrobot; we choose $L = 4.8\,\mu m$ in this paper.

Other microrobots can be designed to act as a basic platform to mount various micro-tools for potential actuation purposes or functional sensors for micro-fluidic environment monitoring.

## 2.5. Experiment and Results Analysis

### 2.5.1. Experimental Setup

All micro-robots used for this study were fabricated with two photon polymerization (2PP) (Photonic Professional GT, Nanoscribe). Photoresist (Nanoscribe, IP-L 780) was used for microrobot fabrication. It is bio-compatible and dielectric, with

a refractive index of 1.50, which is higher than the surrounding medium (the refractive index for water is 1.33). The microrobots and their experimental environment are demonstrated in **Figure 5**.

Figure 5a shows the experimental setup, which consists of an Optical Tweezer system (E3500, Elliot Scientific, UK). The glass slide with the printed microrobots was placed on the sample holder. The microrobots were printed on the glass substrate and placed in deionized (DI) water within a spacer. The DI water provided the suitable medium for optical trapping and prevented the microrobots from attaching to the glass slide. Figure 5b illustrates the schematic sketch of the experimental set up for microrobot control. Sonication process was employed to detach the microrobot from the glass substrate (coverslip). After drying the microrobot sample, an optical microscope (Zeiss, UK) can be used to visualize the microrobot array to check the manufacturing quality before conducting the optical manipulation experiments. The images of the microrobots with various depth levels were collected, as shown in Video S18, Supporting Information. The microscopic views of different microrobots are shown in Figure 5c, while different views of the SEM (scanning electron microscope) images of three typical microrobots with different number of arms are shown in Figure 5d.

To verify that the initial poses of the microrobot and the difference between the experimental fabrications do not affect the out-of-plane control relationship curve, four microrobots fabricated on

**ADVANCED
SCIENCE NEWS**
www.advancedsciencenews.com

**ADVANCED
OPTICAL
MATERIALS**
www.advopticalmat.de

different glass slides are utilized for experiments. Several trials of the same robot were tested. The printed microrobots were manipulated by multi-spot OT that can trap and manipulate different objects simultaneously by scanning predetermined points rapidly (60 kHz). More details of the microrobots regarding the overall dimension in different axes, the volume and the 3D printing parameters used for micro-fabrication are demonstrated in Figures S13–S18, Supporting Information.

### 2.5.2. Evaluation Metrics

Several evaluation metrics were used to evaluate the performance of the proposed design, including the success rate, the maximum control range, and the average control range. To obtain the evaluation metrics, video data was used for post-processing. The position of the optical traps can be identified on the video data, while the distance of the two laser spots can be calculated. The definitions of the evaluation metrics are shown as follows:

*Success Rate*: Success rate represents the percentage of the successful trials for the fulfilment of out-of-plane control among all the trials. Successful trials indicated that the out-of-plane rotation motions can be easily observed. Potential situations that can cause failures to the experiments can be summarized as follows: Situation i: The distance of the two optical traps is changing, while the out-of-plane pose of the microrobot cannot be observed ($\|d(t_0) - d(t_0 - 1s)\| > 3\,\mu m$, $\theta(t_0) - \theta(t_0 - 1s) < 10°$), where $t_0$ is the current timestep. Situation ii: The microrobot flips or rotates in other axes in a random way and is out-of-control, though the distance between the two laser spots remains unchanged ($\|d(t_0) - d(t_0 - 1s)\| = 0\,\mu m$, $\theta(t_0) - \theta(t_0 - 1s) > 10°$).

*Control Range*: Control range includes the maximum control range and the average control range. Maximum range represents the maximum out-of-plane rotation angle that can be achieved during all the experimental trials, while the average range represents the average value of the maximum out-of-plane rotation angle of all the experimental trials.

### 2.5.3. Experiment and Results for the In-Plane Control

The experimental results for demonstrating in-plane translation and planar rotation motions of the proposed Robot D under two optical traps are shown in Video S1, Supporting Information. For planar rotation, the use of dual laser spots which are symmetric at the microrobot center in the plane can enable the microrobot to achieve the rotation of the microrobot about the $z$ axis. The range of the planar rotation of the microrobot can reach 360 degrees. As for the planar transportation of Robot B and Robot C, the real-time control results can be viewed in Videos S2 and S3, Supporting Information, respectively.

### 2.5.4. Distributed Force Control Based on Various Characteristic Distance

Experiments are conducted to verify the deviation of the theoretical modeling results and the experimental results of the

out-of-plane rotation based on varying the characteristic distance, as shown in **Figure 6**.

In order to explore the relationship between the characteristic distance controlled by multiple laser spots and the out of plane pose of the microrobot, the real position of the multiple laser spots used for control at the targeted frame for analysis are recorded. The pose of the microrobot can be estimated by comparing the experimental images and the pre-collected multi-poses library.

The manipulation of the microrobot by creating two optical traps and tuning their relative position to enable the out-of-plane rotation of Robot D (one-arm microrobot) is demonstrated, as shown in Figure 6a. The experimental trials indicated that the out-of-plane rotation can be realized with small deviation for the experimental during different trials. The real-time control result can be viewed in Video S4, Supporting Information.

The experimental results of the out-of-plane rotation of Robot C (three-arm microrobot) along $x$ axis can be viewed in Figure 6b, while the out-of-plane rotation of Robot C along $y$ axis can be viewed in Figure 6c, the real-time control results of which can be viewed in Videos S5 and S6, Supporting Information, respectively. The SEM images of the Robot D and Robot C used for the experimental verification are shown in Figures 6d and 6e, respectively.

Based on the experimental results, it can be concluded that although the variation of the control during different trials can be observed, the general control relationship is reasonable. As for the maximum control range, the experimental results were smaller than the theoretical ranges. This may be due to the fact that when the microrobot was rotated with a large range, the trapping force vanished rapidly. Summary for the success rate and control range for the distributed force control based on various characteristic distance is shown in Table S2, Supporting Information.

### 2.5.5. Distributed Force Control based on Various Power Intensity Distribution

Experiments for out-of-plane rotation based on various power intensity distribution were conducted to verify the effectiveness of controlling the position and relative power intensity simultaneously. **Figure 7** illustrates the experimental results for the power intensity distributed control strategy. The SEM image of Robot B with top-down view and side view are shown in Figures 7f and 7g, respectively.

As shown in Figure 7a, the out-of-plane rotation of Robot B can be achieved. Four laser spots are fixed with the relative distance of $2\sqrt{2}L\sin\left(\dfrac{\varphi}{2}\right)$ between each other, while one laser spot is moving. The power intensity of each of the fixed laser spot and the adjustable laser spot is the same ($m = 1$). The real-time control results for Robot B based on power intensity distributed control with $m = 1$ are indicated in Video S7, Supporting Information.

Figure 7b indicates the control of Robot B with a similar laser spot distribution in Figure 7a, while the power intensity of the adjustable laser spot is twice as high as one of the fixed laser spots ($m = 2$). It can be clearly seen that the maximum out-of-plane
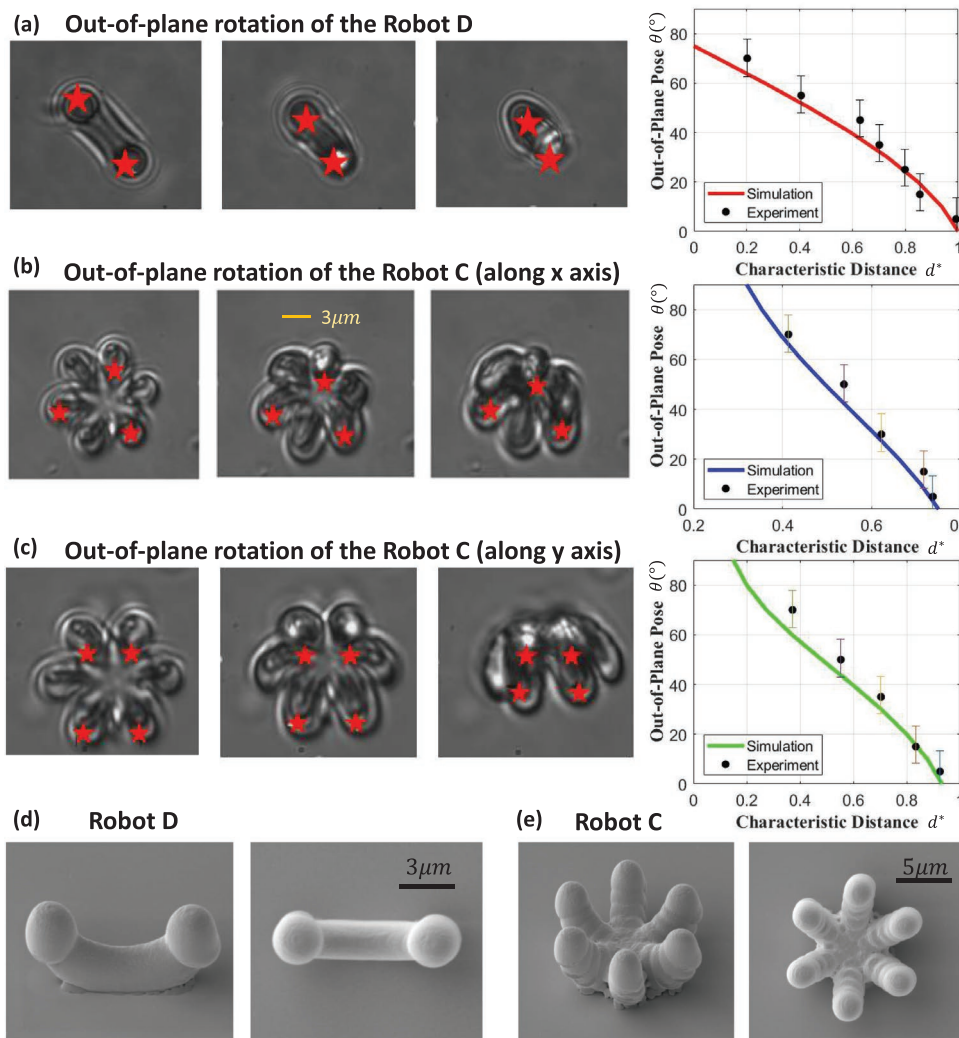
**Figure 6.** Distributed force control for the microrobot rotation along one or multiple axes through characteristic distance (control strategy A) for various microrobots. a) Out-of-plane rotation of the Robot D and comparisons between the experimental results and the theoretical results. b) Out-of-plane rotation of the Robot C along x axis and comparisons between the experimental results and the theoretical results. c) Out-of-plane rotation of the Robot C along y axis and comparisons between the experimental results and the theoretical result. d) The SEM images of Robot D with side view and top-down view. e) The SEM images of Robot C with side view and top-down view.

pose is much larger in this case. The real-time control results for Robot B based on power intensity distributed control with $m = 2$ are indicated in Video S8, Supporting Information.

The theoretical modeling results with parameter tuning and the corresponding experimental results of the control of Robot B based on different power intensity ratio is shown in Figure 7c. The real-time control results for Robot B based on power intensity distributed control with $m = 1.5$ are indicated in Video S9, Supporting Information. It can be concluded that a higher value of $m$ will lead to a higher maximum control range for out-of-plane rotations. However, in practice, $m$ cannot be too big, which may lead to unstable motions during the control and thus influence the success rate. Summary for the success rate and control range for the distributed force control based on various power intensity distribution is shown in Table S3, Supporting Information.

Power intensity distributed control for the one-arm microrobot out-of-plane control is shown in Figure 7d, the real-time control results are indicated in Video S10, Supporting Information. The experimental results of the control of Robot C is shown in Figure 7e when $m = 4$, while the experimental results of the control of Robot C with other parameters are demonstrated in Figure S19, Supporting Information. The real-time control results are indicated in Video S11, Supporting Information. Comparisons between using different power intensities for the moving laser spot are conducted, while the results are shown in Video S12, Supporting Information.

An example of power intensity distributed control for the four-arm microrobot out-of-plane control can be viewed in Video S13, Supporting Information, while the SEM image of the four-arm microrobot is shown in Figure S20, Supporting Information. The results of comparisons when using different
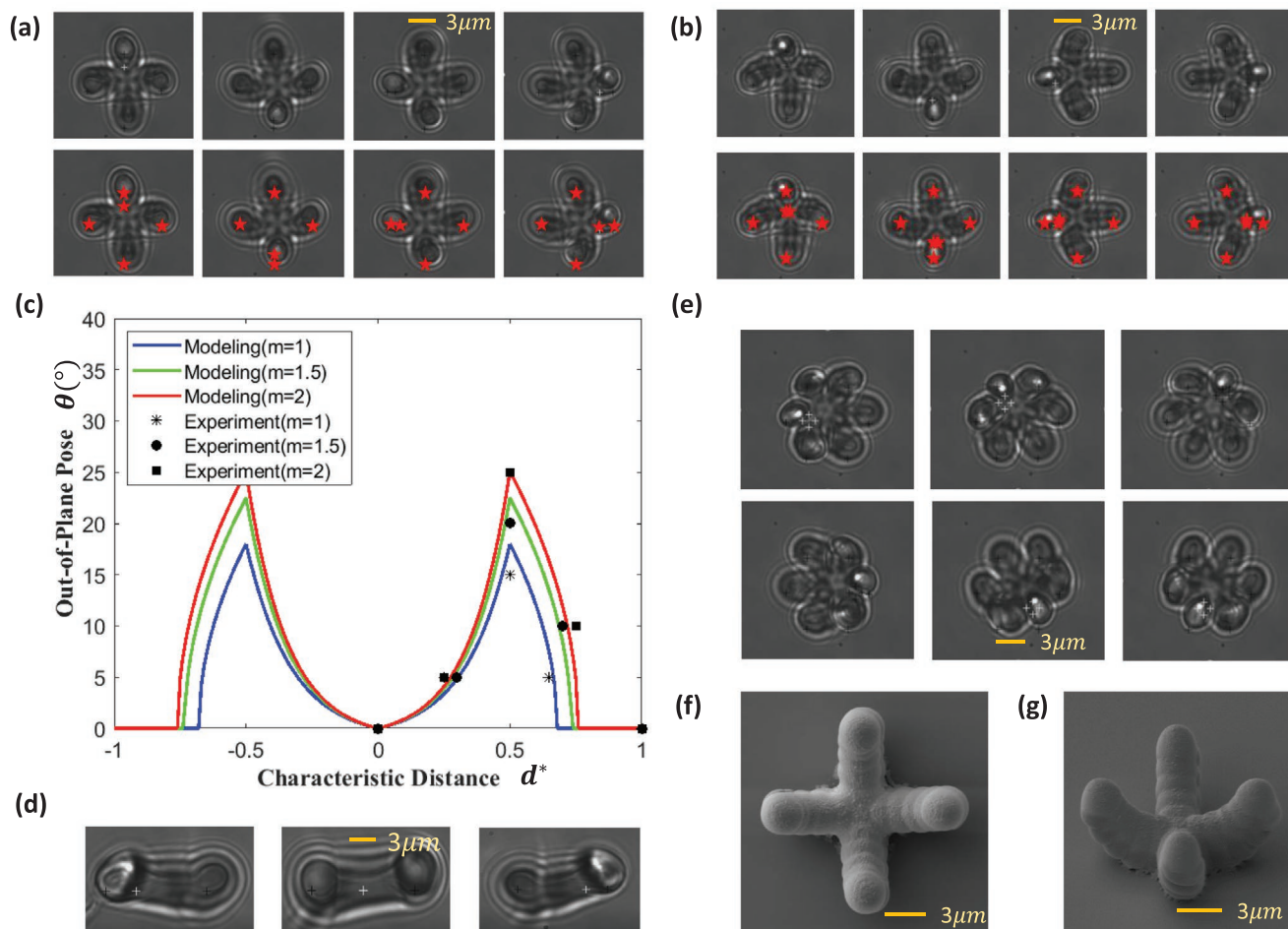
**Figure 7.** Experiments for power intensity distributed control (control strategy B) for various microrobots. a) The validation of control for two-arm microrobot with concept demonstration when $m = 1$. b) The validation of control for two-arm microrobot with concept demonstration when $m=2$. c) Comparisons between different values of $m$. d) Experimental results of the control of one-arm microrobot. e) Experimental results of the control of three-arm microrobot. f) The SEM image of Robot B with top-down view. g) The SEM image of Robot B with side view.

values of $m$ are shown in Video S14, Supporting Information. For $n_b$-arm microrobot, $n_b$ fixed laser spots can be used to transport the robot in the initial status, the relative distance of which is $L\sin\left(\dfrac{\varphi}{2}\right)\sin\left(\dfrac{\pi}{n_b}\right)$.

### 2.6. Experiments for Microrobot Indirect Manipulation

The out-of-plane pose $\theta$ of the microrobot can be adjusted by increasing or decreasing the characteristic distance based on the control strategy A. In order to test whether the changing direction has influence on the control relationship curve of the microrobot or not, comparative studies are conducted. The two control directions are illustrated as follows:

1) Increased distance direction: The increased distance direction assumes that the initial out-of-plane pose of the microrobot is at the maximum out-of-plane pose. By increasing the distance between the two laser spots, the microrobot can realize the out-of-plane rotation by decreasing the out-of-plane pose.

2) Decreased distance direction: The decreased distance direction assumes that the initial out-of-plane pose of the microrobot is at 0°. By decreasing the distance between the two laser spots, the microrobot can realize the out-of-plane rotation by increasing the out-of-plane pose.

The experimental results for the distributed force control of the microrobot with two additional holders and the evaluation of indirect manipulation are shown in **Figure 8**. The comparison between two different control directions based on control strategy A, that is, the decreased distance direction and the increased distance direction, can be viewed in Figure 8a. The SEM image of Robot G with top-down view can be viewed in Figure 8d, while the SEM image for the demonstration of using two microrobots to rotate a micro-object is shown in Figure 8e. The real-time control results can be viewed in Video S15, Supporting Information. As for the out-of-plane rotation based on control strategy B, the real-time experimental results can be viewed in Video S16, Supporting Information.

The comparisons between the experimental results and modeling results of Robot G are shown in Figure 8b, which includes the results for comparisons between two control directions. It can be seen that the out-of-plane rotation can be achieved, while the deviations of the modeling and experimental results are not
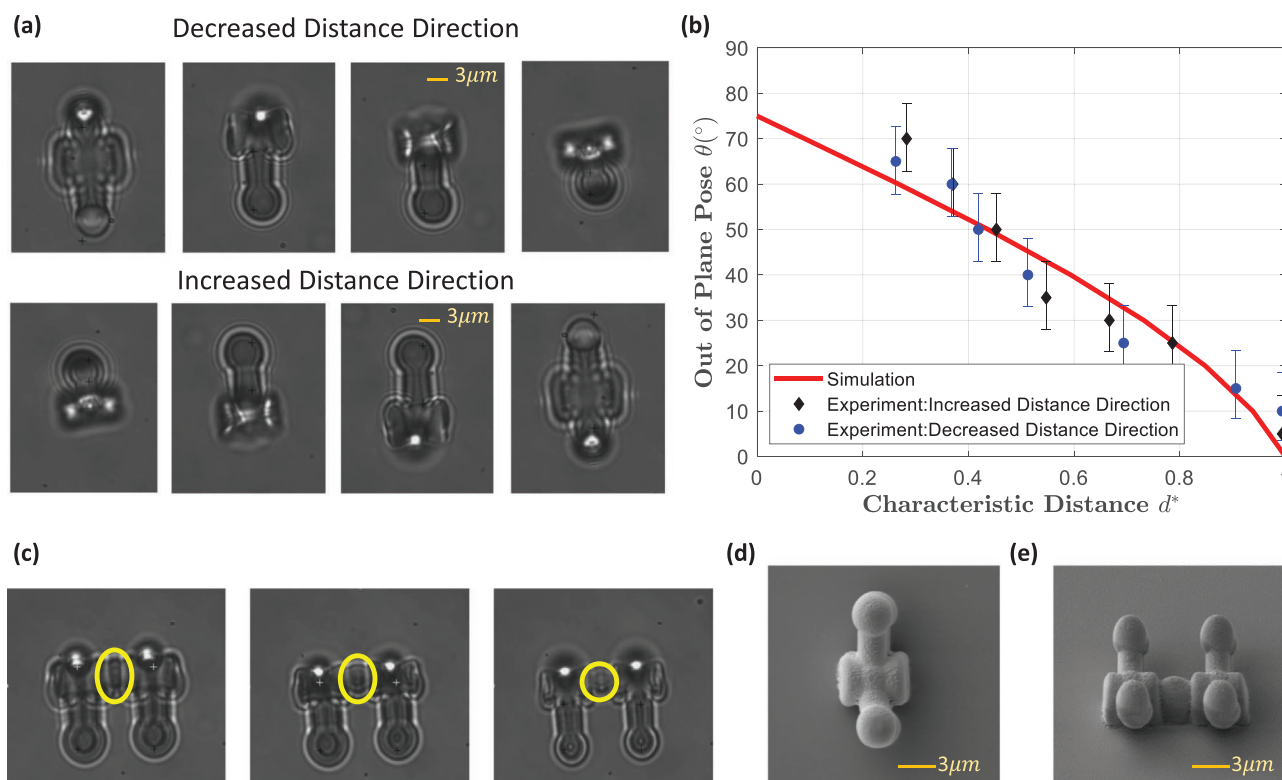
**ADVANCED
SCIENCE NEWS**
www.advancedsciencenews.com

**ADVANCED
OPTICAL
MATERIALS**
www.advopticalmat.de

**Figure 8.** Distributed force control of the microrobot with two additional holders and the evaluation of indirect manipulation. a) Experimental results for the out-of-plane rotation of the Robot G. b) Comparisons between the experimental results and the theoretical results. c) Conceptual evaluation of using two microrobots to rotate a micro-object for observation. d) The SEM image of Robot G with top-down view. e) The SEM image for the demonstration of using two microrobots to rotate a micro-object.

significant. The additional components do not have significant influence on the out-of-plane control properties. Moreover, it can be concluded that the control direction has no significant influence on the control properties.

As for the proof-of-concept application of micro-object examination in the out-of-plane direction, the experimental results are shown in Figure 8c, while the real-time rotation can be viewed in Video S17, Supporting Information. Different views of the micro-object can be observed. The microrobots were printed close to the micro-objects, so the micro-objects can easily be stuck to the holders of the microrobot.

## 3. Discussion

In this paper, several microrobot designs are presented to verify the idea of controlling the out-of-plane pose of the microrobot through adjusting the configuration of the distributed laser-spots of the conventional OT system. Experimental results verified the effectiveness of microrobot transportation via OT, and the out-of-plane rotation can be realized with various initial poses. The out-of-plane rotation in multiple axes can be observed during the experiments when the configuration of the distributed laser spots is changing.

Results have demonstrated that the out-of-plane pose of the microrobot is controllable, though the experimental results and the modeling results have some differences. The mutual influence between the multiple laser spots may cause the deviation

of the results. The control may be inaccurate due to the inherent micro-fabrication errors. However, the overall results indicate the design of the structure of the microrobot for out-of-plane pose control is successful.

As for the two control strategies, they have relative advantages and disadvantages. The characteristic distance based method (control strategy A) can use less number of laser spots, and the overall control range is much larger. However, the stability of this approach is not high, since the center of the power distributed system is moving in a big range for out-of-plane rotation. As for the power intensity distribution based control (control strategy B), the laser spots are redundant. Since the fixed laser spots can form a uniform pattern, the stability of the control can be ensured while the transportation can be conducted with ease. Moreover, the microrobot can rotate in multiple directions easily by changing the power intensity and the position of the moving laser spots. Different control strategies can be used for different applications. For control strategy A, potential applications include micro-assembly in the out-of-plane direction that require stable large rotation angles. As for control strategy B, out-of-plane vibration can be employed for cell characterization purposes.

As for the proof-of-concept validation of using two microrobots to rotate micro-objects, the current limitations include the failure of releasing the micro-objects due to adhesion. Future work will include designing the shape of the gripper for automatic pick-and-place tasks for micro-objects and cell manipulation. The multi-robots cooperative control for

**ADVANCED
SCIENCE NEWS**

www.advancedsciencenews.com

**ADVANCED
OPTICAL
MATERIALS**

www.advopticalmat.de

micro-objects manipulation will be investigated while the dynamic modeling for the interaction between several micro-robots and the targeted micro-objects during micro-manipulation will be considered. The flexibility of the OT system can be further improved by combining magnetic field or acoustic field to provide versatile control of the targeted micro-objects.

## 4. Conclusion

In this paper, multiple in-plane optical traps were used as contactless robotic manipulators' end-effectors. A general mathematical model is used to construct a series of microrobots for the implementation of out-of-plane control along multiple axes, which has potential applications for micro-object manipulation.

Theoretical analysis is conducted to provide the control principle for microrobot out-of-plane manipulation via planar OT. The relationship between the pose of the microrobot and the configuration of the distributed laser spots is investigated. Distributed force control strategies are explored for microrobot dexterous manipulation, including controlling the microrobots based on various characteristic distance and power intensity distribution. Experiments were conducted to verify the effectiveness of the microrobot structure design, including planar transportation and out-of-plane pose control in different axes, respectively.

Experimental results indicate that the proposed structures can achieve the target of out-of-plane rotation along multiple axes, while the two distributed force control strategies have relative advantages and disadvantages. Detailed studies have been conducted to validate the potential of rotating a micro-object cooperatively by using two microrobots, which are formed by the combination of two holders and the basic shape of a microrobot with out-of-plane rotation ability.

Though the out-of-plane poses of the microrobot in different rotation axes can be controlled, the control may be inaccurate due to the inherent micro-fabrication errors. Other errors may originate from the pose estimation. Visual tracking of microrobot will be implemented to track microrobot' position and pose in real-time, which paves the way for high accuracy close-loop control in the future.

## 5. Experimental Section

*Micro Fabrication*: A commercially available 3D printing system (Photonic Professional GT, Nanoscribe) was used to fabricate the microrobots, which relies on the local solidification of a photoresist (Nanoscribe IP-L) at the focus of a laser beam with wavelength of 780 *nm*. By sweeping the laser beam through the photoresist, the 3D structure with features in nanoscale can be built. For this table-top laser lithography system, the lateral resolution was about 200 nm while the vertical resolution was about 300 nm.

A 63x oil-immersion objective was used, where IP-L was on top of glass cover slip and oil was on bottom of glass cover slip. The interface could be found automatically. The dimension of cover slip was $22 \times 22 \times 0.17$ mm, while the dimension of sample tray was $10 \times 30$ mm. During the printing process, sample could be moved by motorized stage for coarse motion and piezo stage for the fine motion. An optical microscope (Zeiss) was used to visualize the process.

The microrobot was generated in a layer-by-layer format. Galvanometric mirror scanner was used for *x–y* directions (horizontal surface). Movement on the *z*-axis was achieved using a piezo stage

to change focus point of laser beam in vertical direction. An array of 100–300 microrobots was fabricated on each glass slide for experiments. The unpolymerized photoresist was washed away by PGMEA (30 min) and cleaned by IPA (2 min), leaving the array anchored to a glass substrate. The array was then immersed in a droplet of 20% water-Tween-20 (Sigma) solution with a space whose diameter was 8 mm.

*Image Pre-processing*: The experimental setup consisted of an Optical Tweezers (Elliot Scientific, UK) with a mounted XYZ-Axis Nanopositioner (Mad City Labs Inc.). The microrobots were imaged through a high-speed CCD camera (Basler AG, Germany) and an oil immersion lens microscope (Nikon Ti) with 100× magnification.

The live video of the microrobot was collected and processed offline. The video of each trial could be converted to images. The resolution of each image frame obtained from the CCD camera was $678 \times 488$ pixels. The transformation between the pixel values and the physical dimensions was calculated by prior registration through cubes with known dimension. All the images that have variation in terms of out-of-plane pose were selected for further analysis. Background subtraction was used to pick up image frames with high variation. In this way, down-sampling of the video data could be realized.

The pose templates of the microrobot with different out-of-plane pose were collected, which constructed a library for template matching by comparing the geometric similarity between the template and the microrobot. A template matching method based on OpenCV was used to assist the out-of-plane pose estimation, which was based on the correlation matrix.

*Dimension Consideration*: For practical consideration, the microrobot cannot be too small to be observed under the microscope or be influenced by Brownian motions during the control process. Moreover, considering the resolution of current 3D micro fabrication technique, the dimension of the microrobot was designed to be larger than 1 μm.

In the meantime, the size of the microrobot was limited due to the fact that the focused laser beam exerting forces ranged from tens of piconewtons down to tens of femtonewtons.[4] Therefore, the size of the microrobot was set to be tens of micron.

## Supporting Information

Supporting Information is available from the Wiley Online Library or from the author.

## Conflict of Interest

The authors declare no conflict of interest.

[1] A. Ashkin, *Phys. Rev. Lett.* **1970**, *24*, 156.

[2] S. Hu, D. Sun, *Int. J. Rob. Res.* **2011**, *30*, 1681.

[3] A. Ashkin, J. M. Dziedzic, *Science* **1987**, *235*, 1517.

[4] D. G. Grier, *Nature* **2003**, *424*, 810.

[5] A. Banerjee, S. Chowdhury, S. K. Gupta, *IEEE Rob. Autom. Mag.* **2014**, *21*, 81.

[6] H. Turlier, D. A. Fedosov, B. Audoly, T. Auth, N. S. Gov, C. Sykes, J.-F. Joanny, G. Gompper, T. Betz, *Nat. Phys.* **2016**, *12*, 513.

[7] T. Wu, T. A. Nieminen, S. Mohanty, J. Miotke, R. L. Meyer, H. Rubinsztein-Dunlop, M. W. Berns, *Nat. Photonics* **2012**, *6*, 62.

[8] B. Li, H. Tan, S. Anastasova, M. Power, F. Seichepine, G.-Z. Yang, *Biosens. Bioelectron.* **2019**, *123*, 77.

[9] D. Palima, J. Glückstad, *Laser Photonics Rev.* **2013**, *7*, 478.

[10] E. Higurashi, H. Ukita, H. Tanaka, O. Ohguchi, *Appl. Phys. Lett.* **1994**, *64*, 2209.

[11] U. G. Būtaitė, G. M. Gibson, Y.-L. D. Ho, M. Taverne, J. M. Taylor, D. B. Phillips, *Nat. Commun.* **2019**, *10*, 1.

[12] S. Zhang, E. Y. Scott, J. Singh, Y. Chen, Y. Zhang, M. Elsayed, M. D. Chamberlain, N. Shakiba, K. Adams, S. Yu, et al., *Proc. Natl. Acad. Sci. USA* **2019**, *116*, 14823.

[13] D. Phillips, M. Padgett, S. Hanna, Y.-L. Ho, D. Carberry, M. Miles, S. Simpson, *Nat. Photonics* **2014**, *8*, 400.

[14] M. Xie, A. Shakoor, Y. Shen, J. K. Mills, D. Sun, *IEEE Trans. Biomed. Eng.* **2019**, *66*, 199.

[15] X. Liu, Z. Lu, Y. Sun, *IEEE/ASME Trans. Mechatronics* **2010**, *16*, 918.

[16] C. Leung, Z. Lu, X. P. Zhang, Y. Sun, *IEEE Trans. Biomed. Eng.* **2012**, *59*, 1049.

[17] L. Feng, P. Di, F. Arai, *Int. J. Rob. Res.* **2016**, *35*, 1445.

[18] X. Liu, Q. Shi, Y. Lin, M. Kojima, Y. Mae, T. Fukuda, Q. Huang, T. Arai, *Small* **2018**.

[19] F. Arai, T. Endo, R. Yamuchi, T. Fukuda, in *Proc. 2006 IEEE Int. Conf. on Robotics and Automation*, IEEE, Piscataway, NJ **2006**, pp. 1390–1395.

[20] R. D. Hanes, M. C. Jenkins, S. U. Egelhaaf, *Rev. Sci. Instrum.* **2009**, *80*, 083703.

[21] E. Gerena, S. Régnier, S. Haliyo, *IEEE Rob. Autom. Lett.* **2019**, *4*, 647.

[22] M. A. Rahman, J. Cheng, Z. Wang, A. T. Ohta, *Sci. Rep.* **2017**, *7*, 1.

[23] A. Atajanov, A. Zhbanov, S. Yang, *Micro Nano Sys. Lett.* **2018**, *6*, 2.

[24] E. Avci, M. Grammatikopoulou, G.-Z. Yang, *Adv. Opt. Mater.* **2017**, *5*, 1700031.

[25] J. Glückstad, *Nat. Photonics* **2011**, *5*, 7.

[26] T. A. Nieminen, H. Rubinsztein-Dunlop, N. R. Heckenberg, A. Bishop, *Comput. Phys. Commun.* **2001**, *142*, 468.

[27] A. Ashkin, *Biophys. J.* **1992**, *61*, 569.

[28] M. Xie, A. Shakoor, C. Wu, *Micromachines* **2018**, *9*, 245.

[29] X. Li, C. C. Cheah, *IEEE Trans. Control Sys. Technol.* **2015**, *24*, 1432.

[30] N. Malagnino, G. Pesce, A. Sasso, E. Arimondo, *Opt. Commun.* **2002**, *214*, 15.

[31] X. Li, C. C. Cheah, S. Hu, D. Sun, *Automatica* **2013**, *49*, 1614.

[32] A. Callegari, M. Mijalkov, A. B. Gököz, G. Volpe, *J. Opt. Soc. Am. B* **2015**, *32*, B11.

**2000543** (15 of 15)